

# Sensor concepts for Industry 4.0

---

**Daniel Le**

DEPARTMENT OF MECHANICAL ENGINEERING  
DIVISION OF PRODUCTION AND MATERIALS ENGINEERING

FACULTY OF ENGINEERING LTH  
LUND UNIVERSITY  
2021

MASTER'S THESIS



LUND UNIVERSITY



# Sensor concepts for Industry 4.0

Daniel Le



# LUND UNIVERSITY

# Sensor concepts for Industry 4.0

© 2021 Daniel Le

*Published by*

Department of Mechanical Engineering  
Division of Production and Materials Engineering  
Faculty of Engineering LTH  
Lund University  
P.O Box 118, SE-221 00 Lund, Sweden

Subject: Production and Materials Engineering (MMTM01)  
Supervisor: Filip Lenrick  
Co-supervisors: Oskar Darselius Berg & Jonas Johansson  
Examiner: Jan-Eric Ståhl  
Code: LUTMDN/(TMMV-5316)/1-44/2021



# Abstract

The next industrial revolution has been denoted by Industry 4.0 and is the continuation of the process of knowledge acquisition and further control over the entire production process which has been evolving since the beginning of the industrialization. A paramount driver of Industry 4.0 is the smart sensor.

In this master's thesis, the first stage of a complete smart sensor will be conceptualized. In industrial applications there is a need to determine the stresses that are present in a material when applying external pressure without using invasive methods. The material that will be investigated is Cr-doped  $\text{Al}_2\text{O}_3$ , i.e. ruby, which is a ceramic with outstanding mechanical properties useful in industrial applications. The doping of  $\text{Cr}^{3+}$  ions grants said material with interesting optical properties. Hence, the first stage of a complete smart sensor consists of verifying both quantitatively and qualitatively the fluorescence shift of the so called R fluorescence lines upon externally applying pressure to the Cr-doped  $\text{Al}_2\text{O}_3$  material by using optical fluorescence spectroscopy. This physical phenomenon is also called the piezo-spectroscopic effect which is a behaviour that could act as a reliable sensor for monitoring the mechanical response of the material non-invasively.

The results were inconclusive as the single crystal ruby acquired internal damage quite early during the piezo-spectroscopic measurements. However, fluorescence spectra was gathered and the R fluorescence lines could reasonably be identified. Ultimately, a fluorescence shift upon externally applied pressure could not be verified quantitatively nor qualitatively. For further work, the experimental setup must improve and conceptualizing a complete sensor for use in the next industrial revolution requires taking into account the effects of temperature and material composition in combination with the piezo-spectroscopic effect.

**Keywords:** Fluorescence, alumina, ruby, piezo-spectroscopic effect

# Sammanfattning

Nästa industriella revolution har kommit att kallas för Industri 4.0 och antas vara en förlängning av den processen som innebär kunskapsinhämtning och ytterligare kontroll av hela tillverkningsprocessen vilken har utvecklats sedan början av den industriella revolutionen. En viktig drivkraft i Industri 4.0 är den intelligenta sensorn.

I denna masteruppsats conceptualiseras det första steget av en fullständig intelligent sensor. Inom industriella tillämpningar finns det ett behov av att bestämma de påfrestningar som föreligger i ett material vid applicering av externt tryck utan att använda sig av invasiva metoder. Materialet som kommer att undersökas är Cr-dopat  $\text{Al}_2\text{O}_3$ , d.v.s rubin, vilken är en keram med utmärkta mekaniska egenskaper som är användbara inom industriella tillämpningar. Genom att dopa med  $\text{Cr}^{3+}$ -joner får det aktuella materialet intressanta optiska egenskaper. Därmed kommer det första steget av en fullständig intelligent sensor bestå av att bekräfta både kvantitativt och kvalitativt fluorescensskiftet av de så kallade R-fluorescenslinjerna vid appliceringen av externt tryck på det Cr-dopade  $\text{Al}_2\text{O}_3$ -materialet genom att använda optisk fluorescensspektroskopi. Detta fysikaliska fenomen kallas även för den piezo-spektroskopiska effekten vilken är ett beteende som kan utnyttjas som en pålitlig sensor för att övervaka den mekaniska reaktionen hos materialet icke-invasivt.

Resultatet var tvetydigt då den monokristallina rubinen ådrog sig interna skador ganska tidigt under de piezo-spektroskopiska mätningarna. Däremot kunde fluorescensspektra erhållas och R-fluorescenslinjerna kunde någorlunda identifieras. Slutligen kunde ett fluorescensskifte vid applicering av externt tryck inte bekräftas varken kvantitativt eller kvalitativt. För fortsatt arbete måste den experimentella ställningen förbättras och conceptualiseringen av en fullständig intelligent sensor för användning i den kommande industriella revolutionen måste ta hänsyn till effekterna av temperatur och materialsammansättning i kombination med den piezo-spektroskopiska effekten.

**Nyckelord:** Fluorescens, aluminiumoxid, rubin, piezo-spektroskopisk effekt

# Acknowledgements

This master's thesis hereby finalizes its author's participation in the five-year master's programme in engineering nanoscience at the Faculty of Engineering LTH, Lund University and has been conducted in collaboration with the department of mechanical engineering, more specifically the division of production and materials engineering.

I sincerely wish to acknowledge and express my gratitude to my primary supervisor, Filip Lenrick, who guided me throughout this project. His help has been invaluable concerning numerous parts of the project, especially during an ongoing pandemic, and without him this master's thesis would have never been finalized. Thank you, Filip.

Due to the ongoing COVID-19 pandemic and its associated restrictions, the accessibility to labs and proper equipment has been kept to a minimum, hence making practical measurements difficult to conduct. Fortunately, professor Zhongshan Li and postdoctoral researcher Wubin Weng gladly offered to help me with the measurements. They too, have made it possible finalizing my master's thesis. For this reason, I also wish to thank Zhongshan Li and Wubin Weng.

I wish to show my appreciation for my co-supervisors Oskar Darselius Berg and Jonas Johansson for participating in my project and suggesting appropriate subjects for a master's thesis. Furthermore, I would like to thank Rachid M'saoubi and Volodymyr Bushlya from Seco Tools AB for giving me inspiration for an appropriate master's thesis subject, and for collaborating with me throughout the project. A thanks to Axel Knutsson from Alfa Laval AB for giving me inspiration as well.

Finally, I wish to extend my gratitude to my managers at the laboratory at Skånemejerier AB, Jenny Hellström and Robin Thörn, for being considerate with me writing my master's thesis whilst working full time simultaneously.



# Contents

<b>1</b>	<b>Introduction</b>	<b>1</b>
1.1	Background . . . . .	1
1.1.1	Industry 4.0 . . . . .	1
1.1.2	Smart sensor technology . . . . .	1
1.2	A brief history of $\text{Al}_2\text{O}_3$ . . . . .	2
1.3	Problem formulation . . . . .	3
1.4	Objectives . . . . .	4
1.5	Limitations . . . . .	5
1.6	Delimitations . . . . .	5
<b>2</b>	<b>Theory</b>	<b>6</b>
2.1	Photolumiscence . . . . .	6
2.1.1	Flourescence . . . . .	6
2.2	$\text{Al}_2\text{O}_3$ and its polymorphs . . . . .	8
2.3	Cr-doped $\alpha\text{-Al}_2\text{O}_3$ . . . . .	8
2.4	The piezo-spectroscopic effect of Cr-doped $\alpha\text{-Al}_2\text{O}_3$ . . . . .	11
2.5	Effects of temperature and composition on Cr-doped $\alpha\text{-Al}_2\text{O}_3$ . . . . .	14
2.6	Measurements of coefficients for stress, temperature and composition . . . . .	16
<b>3</b>	<b>Materiel and methods</b>	<b>17</b>
3.1	Materiel . . . . .	17
3.1.1	Embedding the ruby crystal in epoxy . . . . .	17
3.1.2	Grinding and polishing the ruby crystal . . . . .	18
3.2	Methods . . . . .	20
3.2.1	The experimental setup . . . . .	20
3.2.2	Conducting the piezo-spectroscopic measurements . . . . .	23
<b>4</b>	<b>Results and analysis</b>	<b>25</b>
<b>5</b>	<b>Conclusions</b>	<b>28</b>
<b>6</b>	<b>Further work</b>	<b>29</b>



# 1 Introduction

## 1.1 Background

### 1.1.1 Industry 4.0

With its introduction in Germany in 2011, "Industrie 4.0" denoted the fourth industrial revolution and has become the subject of a global world encouraging the digitalization of manufacturing [1]. Industry 4.0 is, however, more of a political vision than it is a technology paradigm. This vision could be described as the continuation of the process of achieving more knowledge and control over the complete production process which has been ongoing since the beginning of the industrialization [2]. Although most of the technologies of Industry 4.0, such as internet of things (IoT) and artificial intelligence, are already in use, many companies still lack insight into the variety of technology offered by Industry 4.0 that provide intelligent components [1].

In traditional manufacturing, applications are stand-alone and separate, and most importantly, they lack the intelligent capabilities such as automated monitoring. Furthermore, the value chain consisting of characteristic and independent steps such as product development, manufacturing, marketing, and logistics results in a poor integration of digital systems. Hence, traditional manufacturing is inefficient. In contrast, the design philosophies of Industry 4.0 include advanced manufacturing systems e.g. intelligent, and agile manufacturing strategies which have the potential to overcome the inconveniences of the traditional manufacturing. These schemes characterize Industry 4.0, where machines and products are an integral part where human interference is minimised [1].

### 1.1.2 Smart sensor technology

An important driver of Industry 4.0 is smart sensor technology [3]. The trend toward smart sensors has since long been associated with better performance, higher integration and sensing of multiple parameters simultaneously [2]. The implementation of smart sensors combined with increased computational power will enable innovative ways to analyse data and gain insights to proactive improvements of various areas of operations. The impact of smart sensors on a firm's performance will be primarily through cost savings. Smart sensors will increase the production flexibility and worker responsiveness by the optimization of the utilization of Just-In-Time processes. Additionally, they will be able to reduce the equipment downtime through predictive maintenance. This can be realized by a well-integrated use of smart sensor system where data collection can enable self-monitoring and self-calibrating equipment, thus improving the

reliability whilst reducing maintenance costs. Moreover, smart sensors have the capability to improve the quality control and reduce waste. Industries where waste is prevalent might benefit the most. As a part of the quality control process, it will also be possible to reduce the amount of non-compliant products. Lastly, smart sensor technology could increase the understanding of cost structures. One of the most important opportunity associated with smart sensor technology is a firm's increase of understanding the factors affecting unit profit and loss throughout production. In combination with real-time data collection, smart sensors could provide a firm insight into the margins associated with individually sold unit and thereby help optimizing the consumption of energy and materials [3].

## 1.2 A brief history of $\text{Al}_2\text{O}_3$

The invention of the jet engine was made possible due to advancements of heat-resistant structural alloys during 1930s and 1940s. Military need for advanced jet engines and industry demand for gas turbines fuelled the development of new alloy compositions which had the potential to push the temperature capabilities and mechanical strength of turbine blades [4]. However, with ambitions to further improve the engine thrust power and fuel efficiency, alloys alone could not meet the requirement of more advanced jet engines. Therefore, in the early 1940s, NASA scientists proposed to coat the heat-resistant alloys, called superalloys, with thermal barrier coatings (TBCs) [4, 5]. In the 1960s ceramic coatings were adopted to its new prototype rockets and planes. As plasma spray (PS) and electron-beam physical-vapor deposition (EB-PVD) techniques were improved during the 1970s and early 1980s, TBCs were applied to civil jet engines. The use of TBCs allows the gas temperatures in gas-turbine engines to be above the melting temperature of a nickel-based superalloy [4].

As seen in figure 1, a TBC system comprises three structural layers, each having different materials and therefore different properties in order to serve their intended functions. The top layer consists of a ceramic coating for thermal insulation. The underlying superalloy substrate offers structural support and the bond coat in between acts as a bonding and oxidation-resistant layer [4]

Exposed to high temperature, a thermally grown oxide (TGO) layer inevitably grows between the ceramic topcoat and the bond coat. Ideally, if the TGO layer is based on continuous, compact and adherent  $\alpha\text{-Al}_2\text{O}_3$ , it could act as an excellent diffusion barrier to prevent inward diffusion of oxygen and hence, further oxidation of the bond-coat and [4, 6]. This is especially important to consider as the thickness and the morphology of the TGO has critical implications on the TBC system and its spallation lifetime [4].

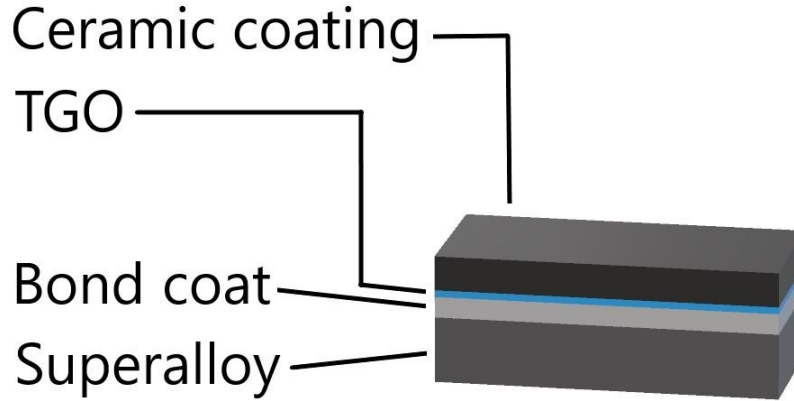


Figure 1: The structure of the thermal barrier coating (TBC) system. The top layer is a ceramic coating and the underlying superalloy provides structural support. The bond coat is a bonding and oxidation-resistant layer. A thermally grown oxide (TGO) layer naturally grows between the ceramic topcoat and the bondcoat upon exposure to high temperature.

However, beyond gas-turbine engines and TBC systems, because of its mechanical properties,  $\text{Al}_2\text{O}_3$  is often used in other diverse engineering applications which includes electronics industry, wear resistant parts, corrosion resistant parts and chemical processing [7]. In fact,  $\text{Al}_2\text{O}_3$  is one of the most used advanced ceramics [8, 9]. This material consists of high ionic inter-atomic bonds, resulting in high chemical stability, thereby functioning as a proper electrical insulator.  $\text{Al}_2\text{O}_3$  is exceptionally resistant to wear and corrosion, and has terrific mechanical strength [8].

### 1.3 Problem formulation

Sensors used in today's industry measure physical quantities such as temperature, pressure, corrosion, oxidation, flow, mechanical deformation and displacement. Extensive research has been done on this matter. For instance, Raman spectroscopy and photoluminescence spectroscopy have contributed to the identification and characterization of materials [4, 10]. By measuring material behaviour such as thermal, mechanical, and electrical attributes, said spectroscopy methods have improved the design of high-performance materials. Spectral peaks are of great interest for understanding how mechanical properties e.g. material degradation and failure under load, work. Photoluminescence spectroscopy is an attractive method because it enables the monitoring of stress changes under real-time loading non-invasively [10].

As  $\text{Al}_2\text{O}_3$  is frequently used in industrial applications, and although taken into account its exceptional mechanical attributes,  $\text{Al}_2\text{O}_3$  is susceptible to mechanical stress, thus inevitably leading to deformation eventually. Therefore, said mechanical stress is necessary to monitor before the deformation occurs. The problem is, invasive methods to monitor such stress are, as the name itself suggests, inherently destructive. Therefore, it is highly relevant to monitor the mechanical response to external stress of  $\text{Al}_2\text{O}_3$  using non-invasive methods integrated in a sensor.

## 1.4 Objectives

This project was created with the purpose of conceptualizing a proof-of-concept sensor for industries such as Seco Tools AB, where components and parts for manufacturing and processing require e.g. high mechanical strength. This decision was based on the ongoing fourth industrial revolution and the resulting need of a higher degree of an integrated value chain with the help of smart sensor technology. However, in this project, a complete sensor will not be realized as this requires more time and resources. Thus, this will not be an objective of this project. Instead, *proof-of-concept* will be synonymous with proving and verifying an existing method to measure a physical quantity.

There are several methods to measure different kinds of physical quantities. Nevertheless, there is a need to determine the stresses that are present in a material without applying destructive methods. In this project the material investigated will be Cr-doped  $\text{Al}_2\text{O}_3$ , i.e. ruby. Doping  $\text{Al}_2\text{O}_3$  with  $\text{Cr}^{3+}$ -ions gives ruby its characteristic reddish fluorescence upon illumination. The method used in this project comprises measurements using optical fluorescence spectroscopy. More specifically, a non-invasive and in-situ measurement system for measuring stresses in Cr-doped  $\text{Al}_2\text{O}_3$  will be conceptualized in this project. This will be done by illuminating said material with a green laser whilst applying an external stress e.g. pressure, after which the so-called piezo-spectroscopic effect, theoretically and hopefully practically, causes a shift in the fluorescence lines which will be measured and compared with a reference fluorescence spectrum. The objective of this project is to verify, both quantitatively and qualitatively, the shift in fluorescence as this will be the first stage of conceptualizing a complete sensor.

## 1.5 Limitations

This master's thesis was conducted during the COVID-19 pandemic and has resulted in limitations associated with the inadequate availability of laboratories, thus making practical experiments difficult to carry through. Not only that but the ongoing pandemic limited my physical presence in the labs which is why a third party consisting of professor Zhongshan Li and postdoctoral researcher Wubin Weng kindly offered themselves to arrange the experimental setup for me. This, of course, limited my power in controlling the methods and outcomes of the experiment but I could have not, in any case, managed the experimental setup better than them considering their experience and knowledge.

Additionally, the fluorescence properties of ruby varies with its Cr-composition and crystallinity. The supply of ruby and not least the amount of suppliers of ruby were limited, hence making the purchase of ruby with certain specifications rather confined and limited. For example, the mechanical and optical properties of single crystal ruby differ from those of polycrystalline ruby, but as only single crystal ruby was available at the time of writing this, only single crystal ruby was purchased. Ergo, this confined the theory to single crystal ruby but fortunately the objectives of this master's thesis is merely proving and verifying the shift of fluorescence lines, and not necessarily comparing fluorescence properties between single crystal and polycrystalline rubies, although a discussion about this might occur.

## 1.6 Delimitations

Ideally, temperature and composition measurements were to be done in combination with piezo-spectroscopic measurements. However, considering the length of this master's thesis (approximately 20 weeks), the limited accessibility to labs and other restrictions regarding the COVID-19 pandemic, such measurements were intentionally omitted. Moreover, a complete sensor was deliberately not conceptualized due to the limited time available.

# 2 Theory

## 2.1 Photoluminescence

Photoluminescence is a physical phenomenon in which a substance absorbs photons whereafter it re-emits photons. Photoluminescence spectroscopy is a method which analyses the distribution of energies involved in the photoabsorption and photoemission processes, the efficiency of the emission process and the temporal characteristics. Taken into consideration the non-invasive and contactless properties, photoluminescence spectroscopy applies to e.g. solids, solutions and gaseous media, hence making it a versatile and sensitive method for structural analysis [11].

Photoluminescence is divided into two forms – fluorescence and phosphorescence – depending on the nature of the excited state. An electronic ground-state orbital occupied by a pair of electrons with opposite spins, is said to be in a singlet state. In fluorescence, the electron in the excited state is paired with the opposite spin electron in the ground state orbital. Consequently, the recombination to ground state is spin allowed and takes place instantly through photon emission. In contrast, phosphorescence is the emission of photons from triplet excited states, which are states occupied by electrons with the same spin orientation as the ground state electron. Therefore, transitions to the ground state are forbidden and the emission rates are slower than those of fluorescence. The lifetime can be quite long which can be manifested in e.g. "glow-in-the-dark" toys [12].

Henceforth, only fluorescence will be elaborated as that is the physical phenomenon investigated in this project.

### 2.1.1 Fluorescence

Fluorescent molecules and materials vary in shape and size. Common fluorescent samples include molecules and materials such as fluorescent proteins, semiconductors and rare earth elements [13].

Fluorescence is a three-stage process and is illustrated by a simple electronic state diagram, also known as Jablonski diagram [14], in figure 2.

In the first stage, a photon of the energy  $h\nu_{ex}$  supplied by an external source, such as a laser, is absorbed by the fluorescent media originally being in the ground state  $S_0$ , consequently producing an excited electronic state,  $S_1$  [14].

In the second stage, the excited media undergoes conformational changes and is

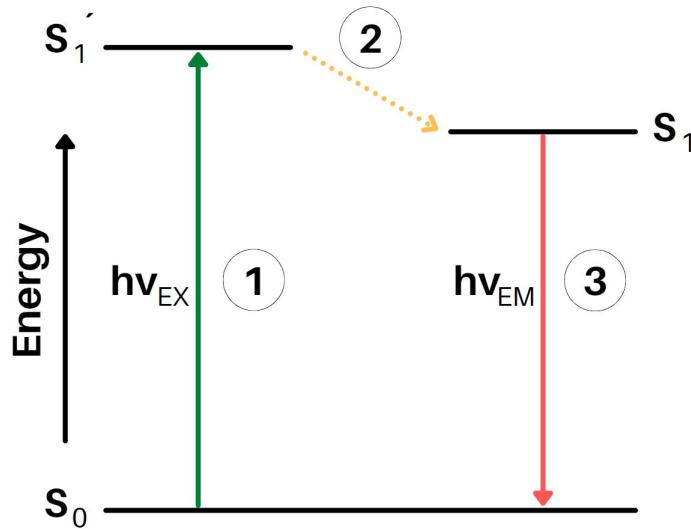


Figure 2: Jablonski diagram displaying the three-stage fluorescence process. The fluorescent media, initially being in the ground state  $S_0$ , is excited by  $h\nu_{ex}$ , thereby producing the excited electronic state,  $S_1'$ . Through mainly heat dissipation, a singlet excited state,  $S_1$  is generated. Lastly, the media returns to its ground state through fluorescence, thus emitting a photon of the energy  $h\nu_{em}$ .

also subject to a group of possible interactions with its molecular environment. This occurs during a finite lifetime of, typically, 1-10 nanoseconds. These possible interactions have two important outcomes. Firstly, the energy of  $S_1'$  is partially dissipated through heat loss to the environment, generating a singlet excited state,  $S_1$ , from which fluorescence emission eventually occurs. Secondly, the excited electronic states do not necessarily return to the ground state  $S_0$  by fluorescence emission. The depopulation of  $S_1$  might occur through non-radiative dissipation processes such as collisional quenching and fluorescence resonance energy transfer (FRET) [14].

In the third stage, a photon of energy  $h\nu_{em}$  is emitted, thus returning the excited media to its ground state  $S_0$ . Due to energy dissipation going from  $S_1'$  to  $S_1$ , the energy of the emitted photon is lower and consequently, the wavelength is longer than that of the excitation photon. The difference in energy, or wavelength, denoted by  $h\nu_{ex} - h\nu_{em}$  is called the *Stokes shift*. The Stokes shift is essential to fluorescence techniques because it allows for the detection of photon emission isolated from excitation photons [14].

## 2.2 Al<sub>2</sub>O<sub>3</sub> and its polymorphs

Al<sub>2</sub>O<sub>3</sub>, also called alumina/aluminium oxide, is an essential ceramic material for technological applications [8, 9]. Specifically, it is Al<sub>2</sub>O<sub>3</sub> corundum, i.e.  $\alpha$ -Al<sub>2</sub>O<sub>3</sub>, that is frequently used in industrial contexts due to its exceptional mechanical properties. It is also the most thermodynamically stable phase of Al<sub>2</sub>O<sub>3</sub>. Nevertheless, there are other metastable phases ( $\kappa$ -,  $\theta$ -,  $\delta$ -,  $\gamma$ -,  $\eta$ - and  $\iota$ -Al<sub>2</sub>O<sub>3</sub>) of technological importance [9]. These metastable phases of Al<sub>2</sub>O<sub>3</sub> will, however, not be further described as  $\alpha$ -Al<sub>2</sub>O<sub>3</sub> will be investigated in this master's thesis. Moreover, it is single crystal  $\alpha$ -Al<sub>2</sub>O<sub>3</sub> that will be investigated as opposed to the polycrystalline equivalent. Of course, an implication of this is a difference in mechanical properties. Polycrystalline materials have grain boundaries which grant polycrystals higher strength and hardness compared to that of single crystals. So, the grain boundaries act as a threshold to dislocation motions [15].

## 2.3 Cr-doped $\alpha$ -Al<sub>2</sub>O<sub>3</sub>

Doping Al<sub>2</sub>O<sub>3</sub> corundum by substitution of Cr<sup>3+</sup> for Al<sup>3+</sup> results in the formation of ruby [9, 16], which comprises parallel sheets of triangularly coordinated O<sup>2-</sup> ions. The Al<sup>3+</sup> ions are coordinated in pairs and occupy 2/3 of the octahedral interstices that are between the sheets [16].

The sheets are perpendicular in respect to the  $c$  axis, i.e. the [0001] direction, of the crystallographic structure and parallel to three equivalent  $a$  axes, denoted by  $a_1$ ,  $a_2$ ,  $a_3$ , lying in the  $\{2\bar{1}\bar{1}0\}$  plane. Furthermore, the axes are separated by 120° and perpendicular to the  $c$  axis. The corundum structure is trigonal but has often been approximated as hexagonal. For convenience, a nonequivalent  $m$  axis parallel to the sheets, lying in the  $\{0\bar{1}\bar{1}0\}$  plane and perpendicular to  $a_1$ , such that  $a$ - $m$ - $c$  form a right-handed, perpendicular coordinate system is introduced [16].

An illustration of the crystallographic construction of the ruby crystal is shown in figure 3 (a). The triangles are rotated 176° relative to each other. Therefore, the interstices are comprising trigonally distorted octahedra constructed by two triangles of O<sup>2-</sup> ions in adjacent sheets. In corundum, the Al<sup>3+</sup> ions are off-centered in the octahedra, located somewhat closer to the smaller triangles of O<sup>2-</sup> ions parallel to the  $c$  axis, as shown in figure 3 (b). In the crystal structure of ruby, the Cr<sup>3+</sup> ions substitute for some of the Al<sup>3+</sup>, hence being similarly octahedrally coordinated and off-centered. The ionic radii of Cr<sup>3+</sup> ions and Al<sup>3+</sup> ions are 64 nm and 57 nm, respectively. Therefore, the larger size of Cr<sup>3+</sup> ions results in an elongation of the substituted octahedra along the  $c$  axis [16].

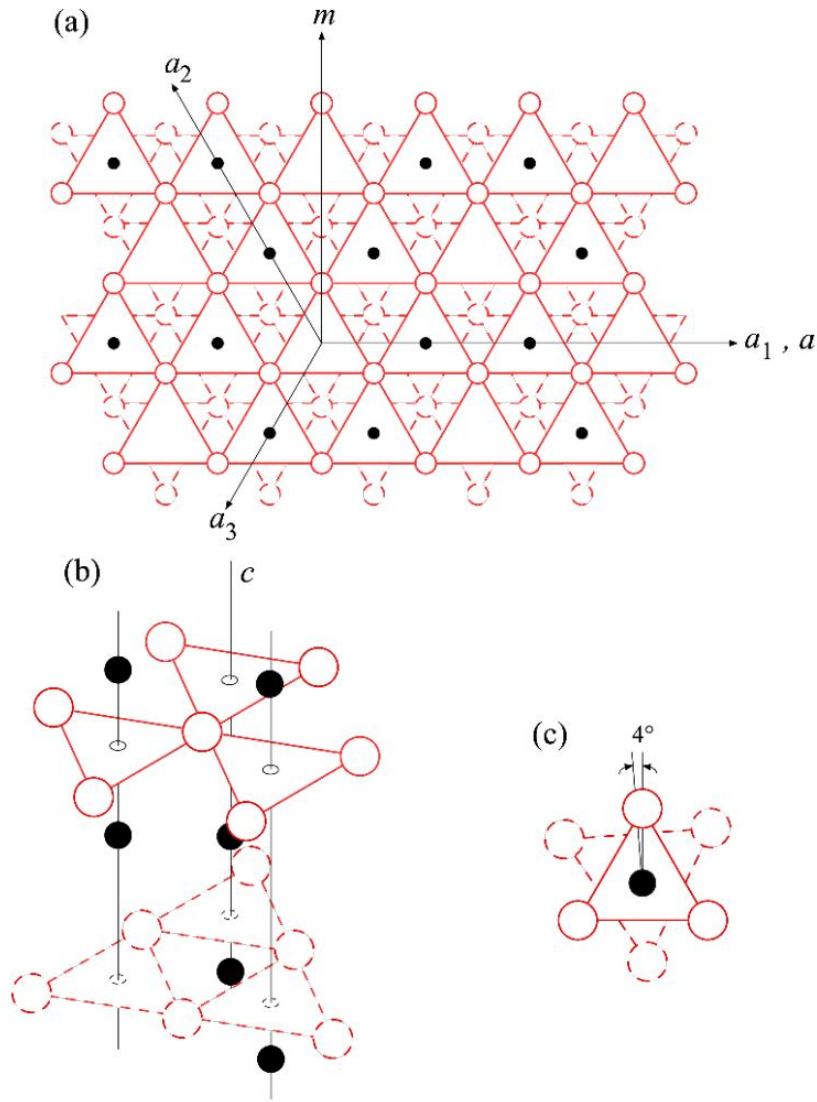


Figure 3: (a) The crystal structure of  $\alpha\text{-Al}_2\text{O}_3$  (ruby) when looking along the  $[0001]$  direction and perpendicular to the equivalent  $a$  axes. The crystal structure comprises triangularly coordinated  $\text{O}^{2-}$  ions (white circles) in sheets that are oriented in an antiparallel fashion along the  $c$  axis (two adjacent sheets are illustrated with solid and dashed lines). The  $\text{Al}^{3+}$  ions (black disks) occupy  $2/3$  of the interstices that are formed between the sheets. (b) Schematic projection of the crystal structure of  $\alpha\text{-Al}_2\text{O}_3$  along the  $c$  axis. (c) Schematic plan view of the trigonally coordinated  $\text{Al}^{3+}$  ions by  $\text{O}^{2+}$  ions, showing the relative rotation of  $4^\circ$  between the lower triangle (dashed) and upper triangle (solid). The figures are adopted from Cook & Michaels (2017) [16].

Cr<sup>3+</sup> ions is an important transition metal member group. The 3d<sup>3</sup> electron configuration of the Cr<sup>3+</sup> ions has an interesting combination of the spin-quartet and spin doublet states. In forming ionic bonds, the transition metals lose their outer 4s electrons and possibly some 3d electrons, such that their consequent electron configurations are 1s<sup>2</sup>2s<sup>2</sup>2p<sup>6</sup>3s<sup>2</sup>3p<sup>6</sup>3d<sup>n</sup> where n<10. Ions having incomplete 3d shells, possess low lying energy levels between which optical transitions may occur. Located outside the ion core, the optically active 3d electrons interact strongly with the electric fields of adjacent ions [17]. In this case, the negatively charged O<sup>2-</sup> ions form an electric field, i.e. a crystal field, at the sites of the Cr<sup>3+</sup> ions, with a nearly perfect octahedral symmetry. The octahedral crystal field results in a low-energy configuration for Cr<sup>3+</sup> ions, consisting of electrons occupying three low energy t<sub>2g</sub> orbitals and two empty, high-energy e<sub>g</sub> orbitals. The three t<sub>2g</sub> orbitals merge into a single ground state denoted by <sup>4</sup>A<sub>2</sub> [16]. Upon incident light, the Cr<sup>3+</sup> ions are excited whereafter electrons are raised from <sup>4</sup>A<sub>2g</sub> to two important excited states in ruby, the <sup>4</sup>T<sub>1g</sub> and <sup>4</sup>T<sub>2g</sub> states, lying around 3.0 eV and 2.2 eV above the ground state <sup>4</sup>A<sub>2</sub>, respectively, as seen in figure 4. Through non-radiative energy dissipation by phonon emission, <sup>4</sup>T<sub>1g</sub> and <sup>4</sup>T<sub>2g</sub> decay to the lowest excited <sup>2</sup>E meta-stable state, which due to spin-orbit coupling, is further divided into two states called  $\bar{E}$  and  $2\bar{A}$  [16, 17].

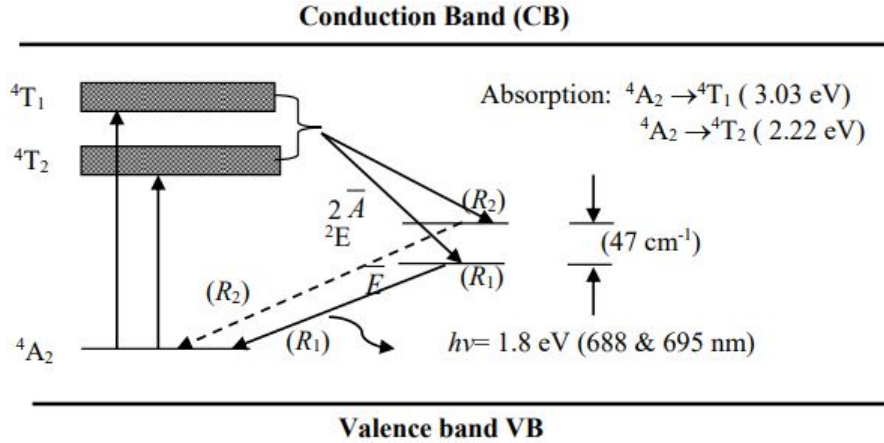


Figure 4: Schematic diagram of the electronic energy levels of Cr<sup>3+</sup> as a doped impurity in  $\alpha$ -Al<sub>2</sub>O<sub>3</sub> (ruby). Upon incident light of adequate wavelength, the Cr<sup>3+</sup> ions are raised to the excited states called the <sup>4</sup>T<sub>1g</sub> and <sup>4</sup>T<sub>2g</sub> states. Through energy dissipation, <sup>4</sup>T<sub>1g</sub> and <sup>4</sup>T<sub>2g</sub> decay to the meta-stable <sup>2</sup>E state. This state is divided into two sublevels from which two transitions are possible, corresponding to 688 nm ( $2\bar{A}$  to <sup>4</sup>A<sub>2</sub>) and 695 nm ( $\bar{E}$  to <sup>4</sup>A<sub>2</sub>). The figure is adopted from Kusuma et al. (2019) [17].

As seen in the schematic energy level diagram of  $\text{Cr}^{3+}$ , two transitions are possible from  ${}^2\text{E}$ : the upper sublevel  $2\bar{A}$  to  ${}^4\text{A}_2$ , and the lower sublevel  $\bar{E}$  to  ${}^4\text{A}_2$  [17].

These two transitions lead to the well known emission lines denoted by  $\text{R}_1$  and  $\text{R}_2$ , i.e. the so called "ruby" lines, which are coincidentally red. The transition from the upper sublevel  $2\bar{A}$ , and the lower sublevel  $\bar{E}$ , to the ground state  ${}^4\text{A}_2$ , correspond to the wavelengths 688 nm ( $\text{R}_2$ ) and 695 nm ( $\text{R}_1$ ), respectively and approximately [16, 17].

## 2.4 The piezo-spectroscopic effect of Cr-doped $\alpha\text{-Al}_2\text{O}_3$

The piezo-spectroscopic effect is a phenomenon where the fluorescence spectrum of a fluorescent material shifts due to strain or stress [18]. Upon photostimulation of the crystal structure of the Cr-doped  $\text{Al}_2\text{O}_3$ , the excited  $\text{Cr}^{3+}$  ions relax to the ground state,  ${}^4\text{A}_2$ , by radiative emission at distinct frequencies such as the "ruby" lines denoted by  $\text{R}_1$  and  $\text{R}_2$ . The  $\text{R}_1$  and  $\text{R}_2$  fluorescence lines correspond to wavenumbers of approximately  $14\,403\text{ cm}^{-1}$  and  $14\,433\text{ cm}^{-1}$ , respectively [16, 18]. The application of external stress renders the interatomic distances in the crystal field, hence changing the potential energy of the  $\text{Cr}^{3+}$  ions which alters the corresponding radiative transitions. In that way, the shifting of the wavenumbers of the  $\text{R}_1$  and  $\text{R}_2$  fluorescence lines are indicative of the reaction of Cr-doped  $\text{Al}_2\text{O}_3$  upon externally applied stress, or strain [18] (as do changes in temperature and composition which alter the octahedra of the crystal [19]). A compressive load on the crystal causes said fluorescence lines to shift to a lower wavenumber whereas a tensile field have an opposite effect, as illustrated in figure 5 [4, 18]. Thus, given the piezo-spectroscopic behaviour of  $\alpha\text{-Al}_2\text{O}_3$ , the shifting of the R fluorescence lines can act as a reliable sensor for monitoring the micromechanical response by calibrating the material to stress, or strain [18].

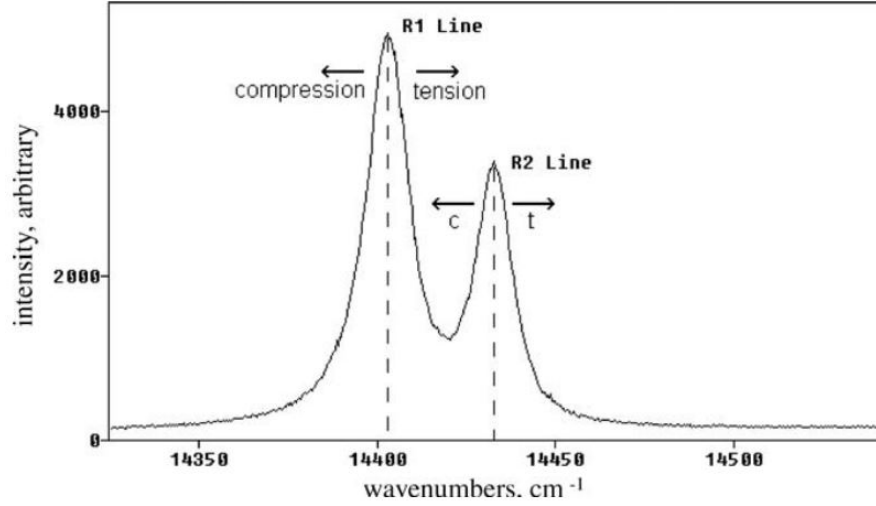


Figure 5: Schematic diagram of the shifting of the wavenumbers of the  $R_1$  and  $R_2$  fluorescence lines upon external stress. A compressive load on the Cr-doped  $\text{Al}_2\text{O}_3$  crystal results in a decrease of the wavenumber of  $R_1$  and  $R_2$ , whilst a tensile field increases the wavenumbers of said radiative transitions. The figure is adopted from Dassios & Galiotis (2004) [18].

All stress components are combined in a symmetric second order stress tensor  $\sigma_{ij}$ , which is not seldom written as a vector. Any stress may be composed of three components, namely uniaxial stress, shear stress and hydrostatic stress. Uniaxial tensile or compressive stresses  $\sigma_{xx}$ ,  $\sigma_{yy}$  and  $\sigma_{zz}$  act along the x,y and z axes, respectively. As seen in figure 6(a), such stresses act normal to the surfaces and their unit is force per area ( $\text{N/m}^2$  or Pa) [20].

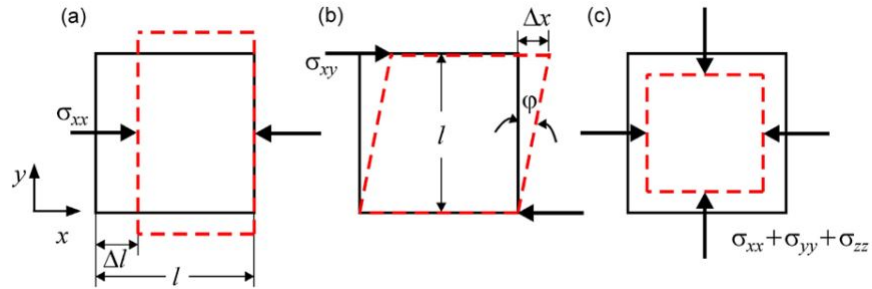


Figure 6: Deformation states of a solid by a) uniaxial stress, (b) shear stress and (c) hydrostatic stress. The figure is adopted from Pohl (2013) [20].

Forces acting tangentially, as in figure 6(b), generate shear stress and are labeled

$\sigma_{xy}$ ,  $\sigma_{yz}$  and  $\sigma_{xz}$ . The first and second index of the stress tensor describe the axis upon which the force acts along, and the normal of the surface where the force acts, respectively [20]. Lastly, hydrostatic stress as in figure 6(c), is a form of stress which comprises uniaxial stresses, but not shear stresses [21].

Quantitative mapping of stress in  $\text{Al}_2\text{O}_3$  relates the measured fluorescence shifts in  $\text{Al}_2\text{O}_3$  to the underlying stress. The basis for the quantitative stress mapping is the correlation between the stress-induced scalar shift in the energy of fluorescence line from a single crystal,  $\Delta v_\sigma$ , and the stress tensor,  $\sigma_{ij}$ , which describes the deformation state of the crystal [19, 22],

$$\Delta v_\sigma = \Pi_{ij}\sigma_{ij} \quad (1)$$

Here,  $\Pi_{ij}$  is the piezospectroscopic coefficient tensor taken in the crystal frame of reference given by that of  $\sigma_{ij}$ .  $\Pi_{ij}$  is a second rank tensor and has symmetry properties given by the site symmetry of the fluorescing  $\text{Cr}^{3+}$  ion. As Cr substitutes Al in distorted octahedra in the corundum structure, the only non-zero terms in  $\Pi_{ij}$  are  $\Pi_{11}$ ,  $\Pi_{22}$  and  $\Pi_{33}$ . Therefore, equation 1 becomes for  $\alpha\text{-Al}_2\text{O}_3$  [19]

$$\Delta v_\sigma = \Pi_{11}\sigma_{11} + \Pi_{22}\sigma_{22} + \Pi_{33}\sigma_{33} \quad (2)$$

As the equivalent  $a$  axes are separated by  $120^\circ$  degrees, there is a three-fold rotational symmetry about the  $c$  (or 3-) axis in the corundum structure, hence leading to an equivalence of the  $a$  and  $m$  (1- and 2-) axes. Assuming this, a conventional notation can be used instead, leading to  $\Pi_{11} = \Pi_{22} = \Pi_a$  and  $\Pi_{33} = \Pi_c$  [19].

## 2.5 Effects of temperature and composition on Cr-doped $\alpha$ -Al<sub>2</sub>O<sub>3</sub>

Aside from external pressure, the temperature and the composition of the corundum structure also affect the shifting of the R fluorescence lines [16, 19, 23]. The effects of stress, temperature and composition are additive and taken as separable terms [16]:

$$\Delta v = \Delta v_{\sigma} + \Delta v_T + \Delta v_C \quad (3)$$

where  $\Delta v$  is the total shift of the center emission peak of one of the R fluorescence lines, and  $\Delta v_{\sigma}$ ,  $\Delta v_T$  and  $\Delta v_C$  are the individual contributions to the total frequency shift, stemming from stress ( $\sigma$ ), temperature ( $T$ ) and composition ( $C$ ). An example displaying this notation is given in figure 7, where the generated frequency shift denoted by  $\Delta v = v - v_0$ , is given by the center emission peak  $v_0$  in an unconstrained system (e.g. a single crystal sapphire) and the measured emission peak  $v$  in a constrained system (e.g. polycrystalline Cr-doped  $\alpha$ -Al<sub>2</sub>O<sub>3</sub>) [16].

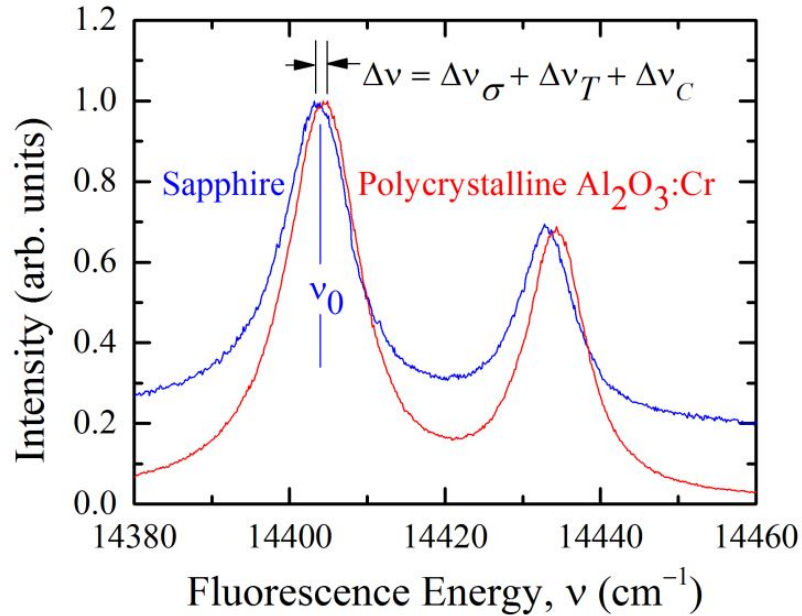


Figure 7: Schematic illustration merely displaying the notation for the effects of stress, temperature and composition on the R<sub>1</sub> and R<sub>2</sub> lines for sapphire and polycrystalline Cr-doped  $\alpha$ -Al<sub>2</sub>O<sub>3</sub>. The figure is adopted from Cook & Michaels (2017) [16].

However, as stress measurement is usually of the most interest, equation 3 is often written as

$$\Delta v_\sigma = \Delta v - \Delta v_T - \Delta v_C \quad (4)$$

where the effects of temperature and composition can be perceived as correction terms [16]. The shift in energy of the R fluorescence lines with changes in temperatures and composition are simply proportionalities. The shift with changes in temperature,  $T(\text{K})$ , is given by [16, 24]

$$\Delta v_T = \beta_T(T - T_{ref}) \quad (5)$$

where  $T_{ref}$  is the reference temperature, normally taken as 298.8 K, and  $\beta_T$  is the proportionality coefficient. Given normal conditions,  $\beta_T$  is negative, meaning with an increase in temperature, the shift in fluorescence energy decreases [16, 24].

The shift in energy of the R fluorescence lines with the composition  $C$ , is given akin to equation 5, but without a reference point, as [16, 24]

$$\Delta v_C = \beta_C C \quad (6)$$

where  $C$  is the composition of Cr in mass fraction in the corundum structure. The proportionality coefficient  $\beta_C$  is positive, meaning with an increase of Cr content, the shift in fluorescence energy also increases [16, 24]. It is worthwhile to mention that  $\beta_T$  and  $\beta_C$  are different for the  $R_1$  and  $R_2$  lines [16].

The crystal field generated by the octahedral arrangement of the  $O^{2-}$  ions and  $Cr^{3+}$  ions in the corundum structure results in two closely-separated R fluorescence lines. The applications of external stress, changes in temperatures and different Cr compositions distort the octahedral arrangement and the associated crystal field, thus leading to energy shifting of the  $R_1$  and  $R_2$  fluorescence peaks [19, 24].

In addition, the crystal structure of the single crystal Cr-doped  $Al_2O_3$  displays anisotropic thermal expansion. The coefficient of thermal expansion (CTE) is greater along the  $c$ -axis, i.e. the [0001] direction, than in the basal plane that contains the three equivalent  $a$  axes,  $a_1$ ,  $a_2$ ,  $a_3$ , lying in the  $\{2\bar{1}\bar{1}0\}$  plane. Consequently, upon cooling an unconstrained single crystal of Cr-doped  $Al_2O_3$ , the  $c$ -axis will contract more than the equivalent  $a$  axes which contract isotropically in the basal plane, leading to an anisotropic stress-free strain state [19, 24]. A stress-free strain state is also called an *eigenstrain*, which is any mechanical deformation in a material that is not a result of an external mechanical stress [25].

## 2.6 Measurements of coefficients for stress, temperature and composition

Cook & Michaels [16] have reviewed external papers covering this very subject, and present the numerical values of the stress, temperature and composition coefficient measurements, i.e. the coefficients  $\Pi_a$ ,  $\Pi_c$ ,  $\beta_T$  and  $\beta_C$  acquired by the authors of these papers. The following subsection presents the numerical values of these coefficients in a similar manner as Cook & Michaels [16] did. The reason for presenting numerical values of the coefficients is to give an overview of the absolute values of the coefficients, thus allowing for reasonable expectations of the coefficients when conducting the stress, temperature and composition coefficient measurements.

In their paper, Cook & Michaels [16] review the stress coefficients acquired by six authors after uniaxial stress loading in the form of quasi-static tests on polycrystalline  $\text{Al}_2\text{O}_3$ , the temperature being unreported but presumably at 300 K. Although single crystal ruby is used in the measurements of this project, the numerical values of the coefficients presented are solely used to give a rough idea on the size of the numerical values. In table 1, the mean values of the stress coefficients acquired from the six authors are presented.

Table 1: Mean numerical values of the stress coefficients for the R fluorescence lines, along different crystallographic orientations, in polycrystalline  $\text{Al}_2\text{O}_3$  as presented in the paper by Cook & Michaels [16]. The unit for the stress coefficients is  $\text{cm}^{-1}/\text{GPa}$ .

<b>Stress coefficients</b>	$\Pi_a^{(1)}$	$\Pi_c^{(1)}$	$\Pi_a^{(2)}$	$\Pi_c^{(2)}$
Mean values	$2.87 \pm 0.06$	$1.65 \pm 0.04$	$2.49 \pm 0.07$	$2.19 \pm 0.07$

Furthermore, Cook & Michaels [16] have reviewed publications reporting on the temperature and composition coefficients. Concerning the temperature coefficients, most reported observations made by the authors of these publications fell in the range  $\beta_T^{(1)} = \beta_T^{(2)} = (-0.140 \pm 0.007) \text{ cm}^1/\text{K}$ . The measurements were done on polycrystalline  $\text{Al}_2\text{O}_3$ , at 300 K [16].

Regarding the composition coefficients, there were not many reports on the effects of the variations in the  $\text{Cr}^{3+}$  ion concentration on the shifting of the R fluorescence lines in  $\text{Al}_2\text{O}_3$ . Despite a few reported numerical values on the composition coefficients, a valid estimation appears to be  $\beta_C^{(1)} = \beta_C^{(2)} \approx (120 \pm 30) \text{ cm}^1/\text{mass fraction}$  [16]. The conditions under which the measurements were conducted are not reported by Cook & Michaels [16].

# 3 Materiel and methods

## 3.1 Materiel

A single cubic crystal ruby with the dimensions 5x5x5 mm, containing 0.9%  $\text{Cr}_2\text{O}_3$ , was purchased from GoodFellow. The ruby crystal was initially opaque and needed polishing before conducting the piezo-spectroscopy experiment; upon shining the laser on the opaque facets of the ruby crystal cube, the monochromatic light would be scattered and therefore disrupt the detectors which is why polishing of the facets is required for the optimal acquisition of the fluorescence spectrum.

### 3.1.1 Embedding the ruby crystal in epoxy

Before polishing it, the ruby crystal was embedded in epoxy using a mounting equipment of the model CitoPress-5 by Struers, as seen in figure 8. This particular model consists of an automatic, electro-hydraulic hot-mounting press with a single cylinder [26]. The reason for embedding the ruby crystal in epoxy is because the dimensions of the crystal were small and the epoxy would facilitate the handling of the crystal.



Figure 8: Mounting equipment used to embed the ruby crystal in epoxy. This model is called the CitoPress-5 and is produced by Struers. The figure is adopted from Struers (n.d) [26].

Before embedding the ruby crystal with the epoxy, the hot-mounting press was treated with a non-stick adhesion. The epoxy used was a hot mounting resin called MultiFast which is a material comprising bakelite with wood filler [27]. The recipe used is shown in table 2.

Table 2: Recipe used for embedding the single crystal ruby in MultiFast epoxy, using the mounting equipment CitoPress-5 by Struers. The recipe is acquired from Struers [27].

Quantity, ml	Heating, min.	Pressure, bar	Cooling, min.	Cooling rate
25	3	250	2	High

After being treated by the CitoPress-5, the single crystal ruby was surrounded by a cylindrical shape of epoxy with a thickness of approximately 1.5 cm, as seen in figure 9.

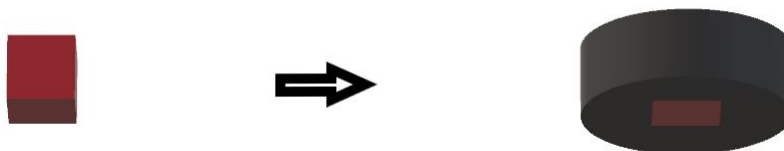


Figure 9: Schematic illustration of the single crystal ruby embedded in Multifast epoxy, using the CitoPress-5 by Struers. The thickness of the epoxy is around 1.5 cm.

### 3.1.2 Grinding and polishing the ruby crystal

Embedded in epoxy, the ruby crystal was ready for polishing. This was done using the grinding and polishing equipment Tegramin-30 by Struers which is an automatic, microprocessor-controlled machine for grinding and polishing, as seen in figure 10.

Before polishing the ruby crystal, the epoxy had to be grinded before the polishing machine could reach the ruby crystal. The same Tegramin-30 used for polishing was also used for grinding. For grinding, an SiC foil #4000 with 10  $\mu\text{m}$  particles was used, whilst applying 10 N for 30 seconds at 150 rpm. The recipe for grinding the ruby crystal is displayed in table 3.

Table 3: Recipe for grinding the epoxy-embedded single crystal ruby, using the grinding and polishing equipment Tegramin-30 by Struers.

<b>Grinding</b>	Force, N	Time, seconds	Speed, rpm
Values	10	30	150



Figure 10: Grinding and polishing equipment used to grind and polish the ruby crystal embedded in epoxy. This model is called the Tegramin-30 and is produced by Struers. The figure is adopted from Struers (n.d) [28].

After grinding the epoxy, the ruby crystal could finally be polished. This was done using a circular polishing cloth MD-Plan with the grid size  $9\ \mu\text{m}$ , whilst applying 40 N for 3 minutes at 150 rpm. This polishing process was repeated three times, hence giving a total polishing time of nine minutes which yielded adequate polishing results. The recipe for polishing is displayed in table 4.

Table 4: Recipe for polishing the epoxy-embedded single crystal ruby, using the grinding and polishing equipment Tegramin-30 by Struers. This recipe was repeated three times for each facet which yielded sufficient polishing results.

<b>Polishing</b>	Force, N	Time, seconds	Speed, rpm
Values	40	180	150

Only one facet of the ruby crystal cube could be polished at a time. Once a facet was polished the epoxy had to be cracked open after which the crystal had to be embedded in epoxy again. The process of embedding the crystal in epoxy, grinding and polishing the crystal was repeated four times such that four facets of the crystal cube were sufficiently polished. The remaining sides of the cube were left unpolished as the cube were to be held statically using said unpolished sides during the coming piezo-spectroscopic measurements. Furthermore, the unpolished sides are opposing facets of the crystal cube, thus allowing it to be held using e.g. a clamp. The treated crystal appears in figure 11.

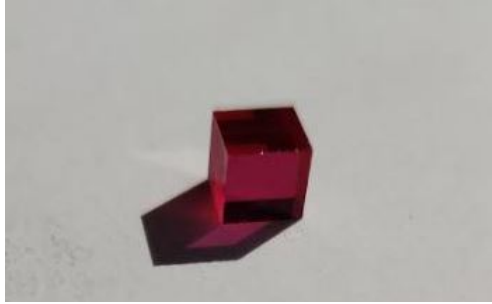


Figure 11: The polished single crystal ruby cube. Four facets are polished whilst two facets remain in opposition to each other and unpolished. One of the unpolished sides appears, in this figure, as the far left facet.

## 3.2 Methods

### 3.2.1 The experimental setup

The application of uniaxial external pressure to the ruby crystal was made possible due to a quite ancient, non-identifiable, type of piston-cylinder apparatus, as illustrated in figure 12. The main components of the apparatus comprise a pressure gauge, a cylindrical piston hidden in the compartment directly below the pressure gauge and a handle used to lower the cylindrical piston. The apparatus was said to be several decades old which is why the units of the pressure gauge are rather unrecognizable: 1 *to* equals to  $20 \text{ kp/cm}^2$ , which in turn equals to approximately 2 MPa. It is of great importance to mention that the displayed pressure on the pressure gauge is misleading as it does not take into consideration the contact area of the ruby. The pressure gauge is rather calibrated according to the contact area of the cylindrical piston so it would actually be more representative had the gauge displayed force instead.

Nevertheless, an attempt to calibrate the pressure gauge with respect to the contact area of the ruby crystal will be done. The diameter of the cylindrical piston is approximately 5 cm which makes the contact area of it approximately  $20 \text{ cm}^2$ . So, the applied force per displayed *to* is  $20 \text{ cm}^2 \cdot 20 \text{ kp/cm}^2 = 400 \text{ kp} \approx 4000 \text{ N}$ . The applied pressure per displayed unit of *to* with respect to the contact area of the ruby crystal ( $0.000025 \text{ m}^2$ ) would be approximately 160 MPa.

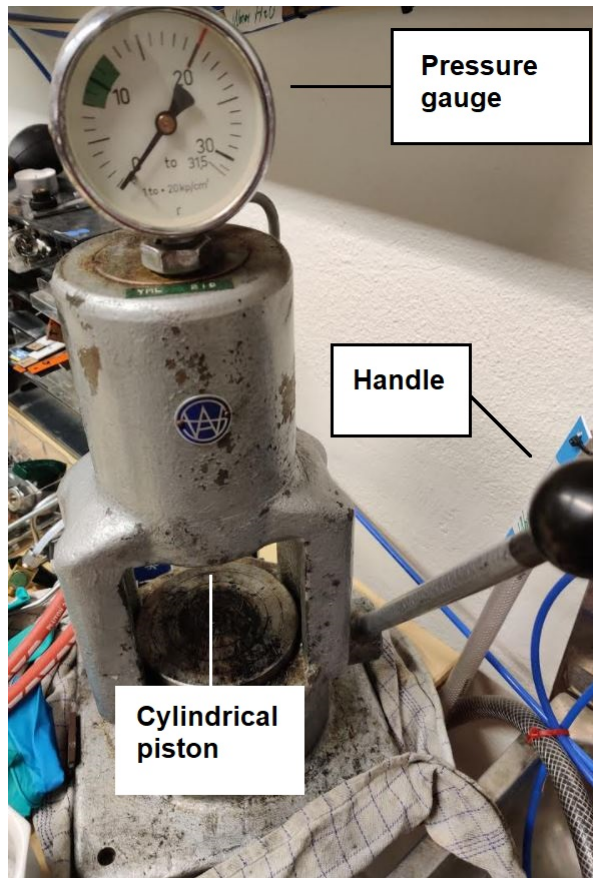


Figure 12: Piston-cylinder apparatus used in the piezo-spectroscopic measurements. It consists of mainly three components: a pressure gauge, a cylindrical piston and a handle. The handle is used to lower the piston on to the hypothetical object situated on the below platform.

The experimental setup was simple in its construction and is displayed in figure 13. The laser system consisted of the model MGL-III-532 by Changchun New Industries Optoelectronics Technology Co., Ltd, and the laser wavelength was  $532 \pm 1$  nm, i.e. a greenish monochromatic light. In the piezo-spectroscopic measurements, an operating power of 25 mW was used. The laser was directed towards the piston-cylinder apparatus, in which the ruby crystal was localized.

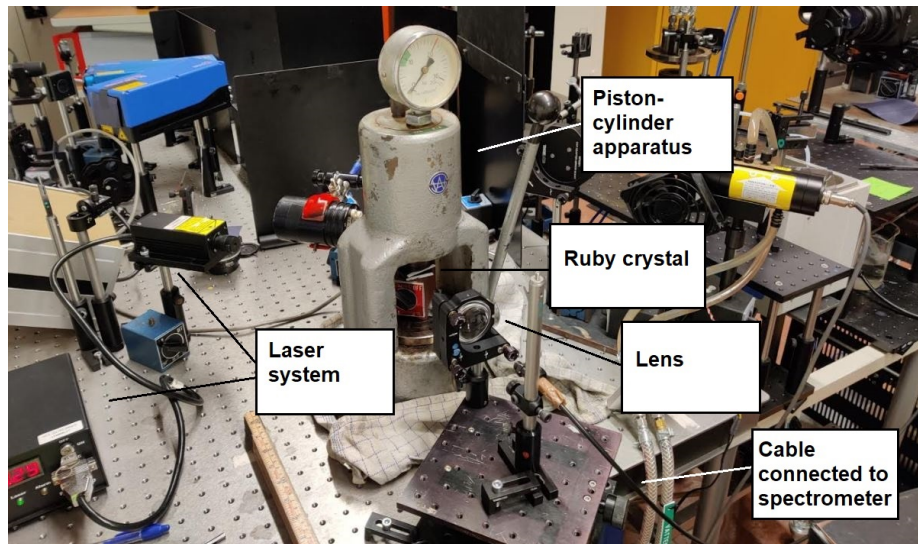


Figure 13: The experimental setup used to conduct the piezo-spectroscopic measurements. It consisted of a laser system of the model MGL-III-532 by Changchun New Industries Optoelectronics Technology Co., Ltd, the piston-cylinder apparatus, a lens, a spectrometer and a computer with the software SpectraSuite.

The ruby crystal was placed firmly on a magnet acting as a platform, as seen in figure 14. The magnet was merely an arbitrary object in order to decrease the distance between the cylindrical piston and the ruby crystal.

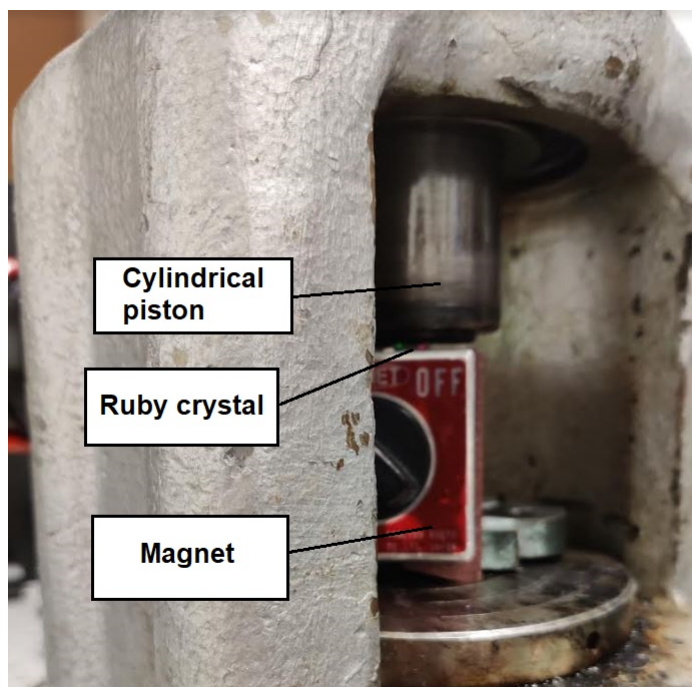


Figure 14: The magnet utilized as a platform for the ruby crystal.

Furthermore, the ruby crystal was initially wrapped in aluminium sheets on the top and bottom facet in order to distribute the pressure homogeneously. However, upon applying external pressure the aluminium sheets deformed quickly which is why they were omitted in the next measurements. The fluorescence was converged using a lens, whereafter a spectrometer of the model USB2000+ by Ocean Optics would analyse it and generate a fluorescence spectrum. The spectrum was displayed on a computer using the software SpectraSuite. Scattered light originating from the ruby crystal was blocked with black paper sheets.

### 3.2.2 Conducting the piezo-spectroscopic measurements

Neither composition or temperature measurements were done due to limited time and restrictions concerning the ongoing COVID-19 pandemic. Instead, only stress measurements were done.

As a means to detect a fluorescence shift upon applying external pressure to the ruby crystal, a reference fluorescence spectrum was required. This was done by disregarding an application of external pressure whilst simultaneously turning the lights off to optimize the acquisition of the fluorescence spectrum.

Given the reference fluorescence spectrum, an external pressure could now be

applied to the ruby crystal whilst acquiring a fluorescence spectrum. The original plan was to acquire a fluorescence spectrum in steps of one displayed unit of  $t_0$  which after calibrated according to the contact area of the ruby crystal instead of that of the cylindrical piston would be 160 MPa, hence the first fluorescence spectrum was acquired when the pressure was increased to 160 MPa. Unfortunately, the last fluorescence spectrum was acquired shortly after, i.e. at 320 MPa, meaning only two fluorescence spectra where external pressure was applied, were measured. This was assignable to the destruction of both the magnet and the ruby crystal. As seen in figure 15, a first glance might reveal the ruby crystal has been pulverized but it has in fact penetrated the underlying magnet which in turn was revealed to be a hollow and poorly built structure. Nevertheless, with the accumulation of cracks and internal damage, the ruby crystal was rendered useless for a new measurement. The data was processed in SpectraSuite and consequently exported to MatLab.



Figure 15: The destruction of the magnet and the ruby crystal. The ruby crystal has penetrated the underlying magnet. The crystal has also accumulated cracks and internal damage.

## 4 Results and analysis

The objective of this project was to verify, both quantitatively and qualitatively, the shift in fluorescence in ruby. Only stress measurements were done as measurements concerning composition and temperature would be too time-consuming, and the restrictions due to the COVID-19 pandemic would make such measurements difficult to arrange.

In figure 16, the combined fluorescence spectrum is displayed. At approximately 533 nm, a spectral peak can be observed. This peak can be assigned to the laser used in the measurements, for which the wavelength was  $532 \pm 1$  nm.

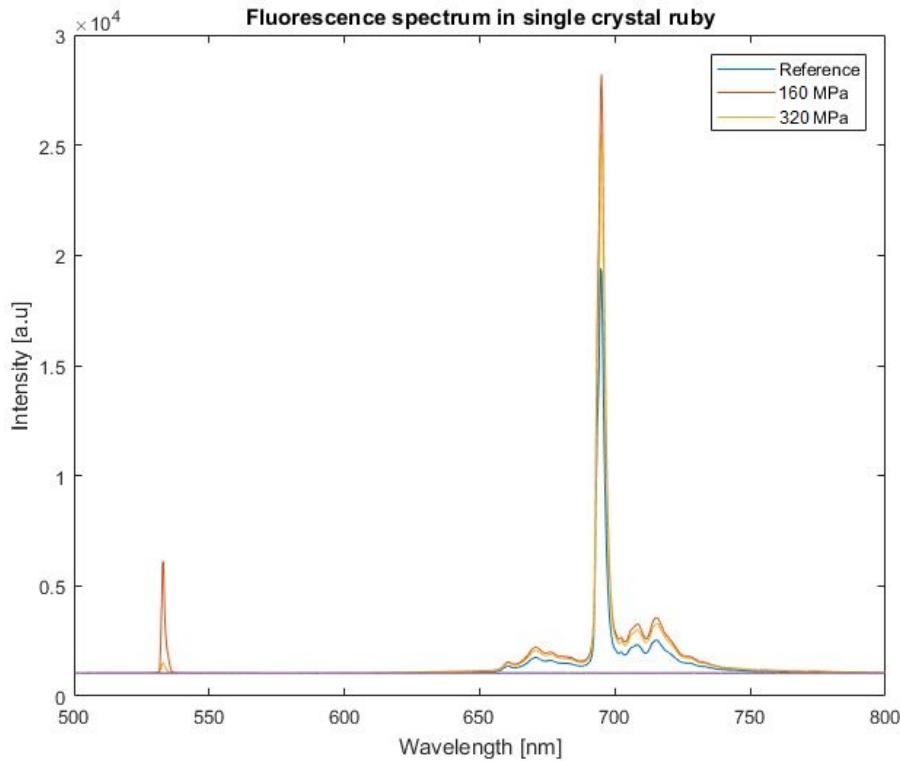


Figure 16: The combined fluorescence spectrum upon applied externally pressure on the single crystal ruby. A reference spectrum was initially acquired after which a fluorescence spectrum was acquired when applying 160 MPa and 320 MPa on the crystal. The peak at around 532 nm is assigned to the laser used in the stress measurements.

In the range of 650 nm to 750 nm, several spectral peaks can be observed. The

ones of relevance and highest interest are those for which the wavelength is approximately 690 nm to 700 nm. In figure 17, said spectral peaks are investigated in-depth. It is quite difficult to identify the R fluorescence lines in the fluorescence spectrum in figure 17. However, there are three spectral lines that are more distinguishable than other ones, and these are marked in the fluorescence spectrum. These three spectral lines are the same for all fluorescence spectra with regards to wavelength. Therefore, and unfortunately, any fluorescence shift upon externally applied pressure uniaxially could not be detected.

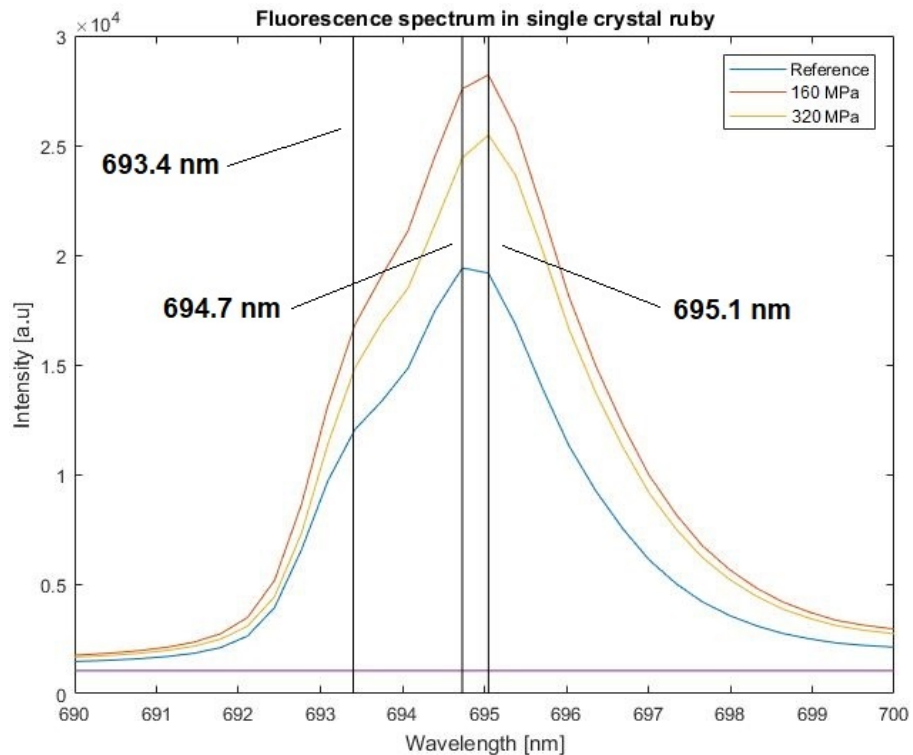


Figure 17: The supposedly R fluorescence lines. Three emission lines have been marked in this combined fluorescence spectrum. The  $R_2$  line should be localized at 693.4 nm ( $\approx 14\,422\text{ cm}^{-1}$ ) whilst the  $R_1$  line is localized at either 694.7 ( $\approx 14\,395\text{ cm}^{-1}$ ) nm or 695.1 nm ( $\approx 14\,386\text{ cm}^{-1}$ ).

Most likely, this is a result of failing to apply a pressure in the range of GPa, which is what is usually done in stress measurement research for polycrystalline Cr-doped  $\alpha\text{-Al}_2\text{O}_3$  according to Cook & Michaels [16]. According to Myers, Michaels & Cook [19] and Michaels & Cook [24], the crystal field caused by the octahedral arrangement of the  $\text{O}^{2-}$  ions and  $\text{Cr}^{3+}$  ions in the corundum structure gives rise to the the R fluorescence lines. The energy shifting of the R fluores-

cence lines must stem from a change in the interatomic distances in the crystal field which in turn changes the octahedral arrangement and the potential energy in the corundum structure [16, 18, 19, 24]. As mentioned before, the applied pressure merely went up to 320 MPa and apparently this amount of pressure was too small to cause any change in the potential energy in the corundum structure. Consequently, a shifting of the R fluorescence lines was not induced. Furthermore, the crystal had already accumulated cracks and internal damage, and penetrated the underlying platform, at as low as 320 MPa such that further pressure applied was deemed useless. It was not expected for the ruby crystal to crack that early during the experiment. However, it is not that remarkable considering the crystal was in a bulk form. As a result, any defects residing in the corundum structure would probably proliferate quickly and lead to damage as opposed to polycrystalline structures which, according to Yang & Park [15], are inherently permeated by grain boundaries such that deformations are greatly hindered. Another reason as to why a shift in the fluorescence spectrum, nor distinctive emission peaks, could not be detected could be attributed to the poor resolution of the spectrometer. Also, as stated by Cook & Michaels [16], the piezo-spectroscopic coefficients vary with the crystallographic direction of the crystal. Because of limited time and equipment, the crystallographic direction of the ruby crystal during the application of external pressure was never verified. Whilst not probable, it could have affected the outcome.

Nonetheless, the first spectral line marked in the fluorescence spectrum has a wavelength of 693.4 nm ( $\approx 14\,422\text{ cm}^{-1}$ ) and should correspond to the  $R_2$  fluorescence line. According to Kusuma et al. [17], the  $R_2$  line corresponds to the transition from  $2\bar{A}$  to  ${}^4A_2$ , meaning an emission of light of 688 nm ( $\approx 14\,535\text{ cm}^{-1}$ ). However, according to Cook & Michaels [16] and Dassios & Galiotis [18], the emitted light has a wavenumber of approximately  $14\,433\text{ cm}^{-1}$ . The measured value of 693.4 nm ( $14\,422\text{ cm}^{-1}$ ) is quite different from 688 nm ( $14\,535\text{ cm}^{-1}$ ) but it is drastically closer to that of Cook & Michaels [16] and Dassios & Galiotis [18]. The discrepancies are probably a consequence of a subpar spectrometer resolution and a prevalence of measurement errors. Although taken these facts into account, the measured value being so close to the theoretical values suggests the marked  $R_2$  line in the fluorescence spectrum is reasonable.

Either of the next two marked spectral lines in the fluorescence spectrum probably corresponds to the  $R_1$  line, i.e. the transition from  $\bar{E}$  to  ${}^4A_2$  according to Kusuma et al. [17]. This is equivalent to an emission of light of approximately 695 nm ( $\approx 14\,388\text{ cm}^{-1}$ ) [17]. According to Cook & Michaels [16] and Dassios & Galiotis [18], the  $R_1$  line corresponds to light emission of  $14\,403\text{ cm}^{-1}$ . The marked wavelengths in the combined spectrum, i.e. 694.7 nm ( $\approx 14\,395\text{ cm}^{-1}$ ) and 695.1 nm ( $\approx 14\,386\text{ cm}^{-1}$ ), are certainly close to the theoretical ones but it is still difficult to actually distinguish between the two spectral lines, and hence identifying the  $R_1$  line, due to the poor resolution of the spectrometer.

## 5 Conclusions

In this project, external pressure has been applied to single crystal Cr-doped  $\text{Al}_2\text{O}_3$ , i.e. ruby, whilst shining green monochromatic light at said material in order to detect a shift in the fluorescence spectrum. This effect is called the piezo-spectroscopic effect. The experimental setup was simple in its construction and consisted of a laser system capable of emitting light of  $532 \pm 1$  nm, a piston-cylinder apparatus, a lens and a spectrometer. The subject of interest has been a single crystal ruby with the dimensions 5x5x5 mm. The ruby crystal was originally unpolished and had to be polished for the purpose of avoiding distortion of the detector, and optimizing the acquisition of the fluorescence spectra. The initial purpose was to apply a pressure in the range of GPa but in the light of the COVID-19 pandemic, the limited access to appropriate equipment and labs has been quite the threshold. In the stress measurements, the pressure increased in steps of approximately 160 MPa. Ultimately, the highest pressure reached was merely 320 MPa before the single crystal ruby accumulated internal damage and had penetrated the underlying platform, hence being rendered useless for further stress measurements. Also, the removal of the crystal from the underlying platform is too difficult and it would probably be destroyed in the process. Totally, a number of three spectra was acquired: one reference, one at 160 MPa and 320 MPa. The results were inconclusive in terms of verifying the piezo-spectroscopic effect.

Additionally, the R fluorescence lines were difficult to identify based on the acquired spectra mainly due to the poor resolution of the spectrometer. Regardless, the  $R_2$  fluorescence line was supposedly determined to have a wavelength of 693.4 nm ( $\approx 14\,422\text{ cm}^{-1}$ ) whilst the  $R_1$  fluorescence line had a wavelength of either 694.7 nm ( $\approx 14\,395\text{ cm}^{-1}$ ) or 695 nm ( $\approx 14\,386\text{ cm}^{-1}$ ).

The objective of this master's thesis was to verify, both quantitatively and qualitatively, the fluorescence shift upon externally applied pressure on the ruby crystal, i.e. the piezo-spectroscopic effect, as the first stage of conceptualizing a complete smart sensor with applications in the fourth industrial revolution. Qualitatively, a fluorescence shift could not be detected due to the failure to reach higher externally applied pressure. The absence of a fluorescence shift meant the stress coefficients, i.e. the piezo-spectroscopic coefficients, could not be determined quantitatively. Measurements concerning composition and temperature were omitted due to lack of time and restrictions concerning the ongoing pandemic.

## 6 Further work

Although the objective was not fulfilled, the stress measurements did generate fluorescence spectra which could be analysed. It was primarily an inadequate experimental setup which led to unsatisfying results. Ultimately, the experimental setup could have been arranged in a different way which would have ensured better results, given that the restrictions would have been kept at its minimum.

Firstly, the single crystal ruby was quickly destroyed during the stress measurements. For future work, a better choice would have been polycrystalline  $\alpha$ - $\text{Al}_2\text{O}_3$ . As Yang & Park [15] describe, polycrystals are mechanically stronger than single crystals due to their grain boundaries. This would allow for higher externally applied pressures without causing destruction to the crystal. It would also be more relevant to investigate polycrystalline  $\alpha$ - $\text{Al}_2\text{O}_3$  as this is the material used in industrial applications, not single crystals. Unfortunately, only single crystal rubies were available for purchase.

Secondly, a spectrometer capable of generating higher resolution data should have been used in the experimental setup which would have allowed for an easier identification of the R fluorescence lines. Concerning the experimental setup, a device capable of generating an externally applied pressure in the range of GPa would have made it possible for verifying the piezo-spectroscopic effect. At the same time, a mechanically stronger underlying platform for the ruby crystal should have been used. The platform should also be fastened so it does not move. An improved experimental setup would lead to more reliable results and an enhanced reproducibility.

Thirdly, it would also have been more relevant to conduct temperature and composition measurements considering that  $\alpha$ - $\text{Al}_2\text{O}_3$  is a material used in industrial applications where mechanical strength is required, and the fact that the composition of the material affects its mechanical and optical properties. By doing this, the benefits are improved industrial applicability and a more reliable monitoring of the stress.

Lastly, further research on this matter is required before this can be applicable in an industrial sense. Ideally, a smart sensor utilizing the piezo-spectroscopic effect should be small in size and portable, yet be highly capable of producing high resolution data. As of now, a bottleneck preventing this optical sensor from crystallizing into a practical smart sensor used in Industry 4.0 is a high resolution yet small spectrometer. That is not to dismiss research regarding the piezo-spectroscopic effect; in fact, much research is still needed before it is possible to measure the fluorescence shift precisely and thus, the stress induced in the  $\alpha$ - $\text{Al}_2\text{O}_3$  material whilst simultaneously taking into consideration the

effects of temperature and composition as well. Besides being non-invasive, a future goal of the smart sensor utilizing the piezo-spectroscopic effect is to be applicable in such harsh industrial environments that would otherwise damage conventional mechanical sensors e.g. strain sensors.

# References

- [1] Tahera Kalsoom, Naeem Ramzan, Shehzad Ahmed, and Masood Ur-Rehman. Advances in Sensor Technologies in the Era of Smart Factory and Industry 4.0. *Sensors*, Vol 20(No 23), 2020.
- [2] Andreas Schütze, Nikolai Helwig, and Tizian Schneider. Sensors 4.0 – smart sensors and measurement technology enable Industry 4.0. *Journal of Sensors and Sensor systems*, Vol 7(No 1), 2018.
- [3] Ernst & Young. Sensors as drivers of industry 4.0: A study on germany, switzerland, and austria, 2019.
- [4] Rudder T. Wu and Liberty T. Wu. A Powerful Tool to Measure Residual Stress in Thermal Barrier Coatings. *IEEE Nanotechnology Magazine*, Vol 11(No 4), 2017.
- [5] Chester T. Sims. A History of Superalloy Metallurgy for Superalloy Metallurgists. *Superalloys 1984 (Fifth International Symposium)*, pages 399–419, 1984.
- [6] JunNan Lv, XueLing Fan, and Qun Li. The impact of the growth of thermally grown oxide layer on the propagation of surface cracks within thermal barrier coatings. *Surface & Coatings Technology*, Vol 309:1033–1044, 2016.
- [7] P.B Parikh. Alumina Ceramics: Engineering Applications and Domestic Market Potential. *Transactions of the Indian Ceramic Society*, Vol 54(No 5):179–187, 2014.
- [8] Sina Ebnesajjad. *Surface Treatment of Materials for Adhesive Bonding*. Elsevier, 2014.
- [9] Michael F. Peintinger, Michael J. Kratz, and Thomas Bredow. Quantum-chemical study of stable, meta-stable and high-pressure alumina polymorphs and aluminum hydroxides. *Journal of Materials Chemistry A*, Vol 2, 2014.
- [10] Gregory Freihofer, L. Poliah, K. Walker, A. Medina, and Seetha Raghavan. Optical stress probe: In-situ stress mapping with Raman and Photo-stimulated luminescence spectroscopy. *Journal of Instrumentation*, Vol 5(No 12), 2010.
- [11] Peter M. Martin. *Handbook of Deposition Technologies for Films and Coatings*. Elsevier, 2010.
- [12] Joseph R. Lakowicz. *Principles of Fluorescence Spectroscopy*. Springer, 2006.

- [13] Horiba. Fluorescence spectroscopy, n.d. Available at: [https://www.horiba.com/en\\_en/technology/spectroscopy/fluorescence-spectroscopy/what-is-fluorescence-spectroscopy/](https://www.horiba.com/en_en/technology/spectroscopy/fluorescence-spectroscopy/what-is-fluorescence-spectroscopy/) [Accessed: 2021-05-30].
- [14] ThermoFisher Scientific. Fluorescence fundamentals, n.d. Available at: <https://www.thermofisher.com/se/en/home/references/molecular-probes-the-handbook/introduction-to-fluorescence-techniques.html> [Accessed: 2021-05-30].
- [15] Guijun Yang and Soo-Jin Park. Deformation of Single Crystals, Polycrystalline Materials, and Thin Films: A Review. *Materials*, Vol 12(No 12), 2019.
- [16] Robert F. Cook and Chris A. Michaels. Coefficients for Stress, Temperature, and Composition Effects in Fluorescence Measurements of Alumina. *Journal of Research of the National Institute of Standards and Technology*, Vol 122(No 43), 2017.
- [17] Hamdan Hadi Kusuma, Budi Astuti, and Z Ibrahim. Absorption and emission properties of ruby (Cr:Al<sub>2</sub>O<sub>3</sub>) single crystal. *Journal of Physics Conference Series*, Vol 1170(No 1), 2019.
- [18] Konstantinos G. Dassios and Costas Galiotis. Fluorescence studies of polycrystalline Al<sub>2</sub>O<sub>3</sub> composite constituents: Piezo-spectroscopic calibration and applications. *Applied Physics*, Vol 79(No 3):647–659, 2004.
- [19] Grant A. Myers, Chris A. Michaels, and Robert F. Cook. Quantitative mapping of stress heterogeneity in polycrystalline alumina using hyperspectral fluorescence microscopy. *Acta Materialia*, Vol 106:272–282, 2016.
- [20] Udo W. Pohl. *Epitaxy of Semiconductors*. Springer, 2013.
- [21] Winston Soboyejo. *Mechanical properties of engineered materials*. Marcel Dekker, 2003.
- [22] Imad Hanhan, Erik Durnberg, G. Freihofer, P.Akin, and S. Raghavan. Portable Piezospectroscopy system: non-contact in-situ stress sensing through high resolution photo-luminescent mapping. *Journal of Instrumentation*, Vol 9, 2014.
- [23] Deirdre D. Ragan, R. Gustavsen, and David Schiferi. Calibration of the ruby R 1 and R 2 fluorescence shifts as a function of temperature from 0 to 600 K. *Journal of Applied Physics*, Vol 72(No 5539), 1992.
- [24] Chris A. Michaels and Robert F. Cook. Determination of residual stress distributions in polycrystalline alumina using fluorescence microscopy. *Materials and Design*, Vol 107(No 5):478–490, 2016.

- [25] Nobuo Kinoshita and Toshio Mura. Elastic fields of inclusions in anisotropic media. *physica status solidi (a)*, Vol 5(No 3):759–768, 2016.
- [26] Struers. Citopress mounting press, n.d. Available at: <https://www.struers.com/en/Products/Mounting/Mounting-equipment/CitoPress#citopressfacts> [Accessed: 2021-05-30].
- [27] Struers. Selection guide for hot mounting, n.d. Available at: [https://publications.struers.com/catalogue/consumables-english/?page=30&\\_ga=2.207329939.1297758897.1622359134-1425724022.1620035203](https://publications.struers.com/catalogue/consumables-english/?page=30&_ga=2.207329939.1297758897.1622359134-1425724022.1620035203) [Accessed: 2021-05-30].
- [28] Struers. Tegramin, n.d. Available at: <https://www.struers.com/en/Products/Grinding-and-Polishing/Grinding-and-polishing-equipment/Tegramin#tegraminfacts> [Accessed: 2021-05-30].